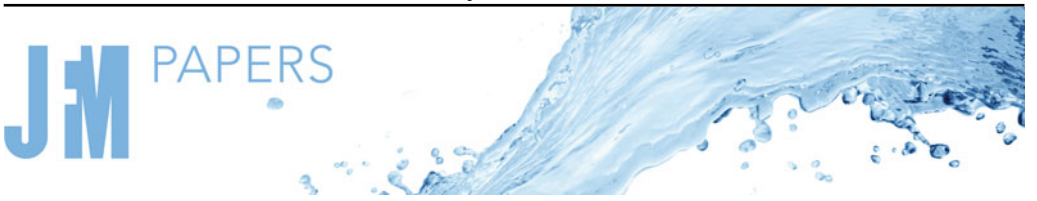
J. Fluid Mech. (2026), *vol.* 1038, A33, doi:10.1017/jfm.2026.11772



Unsteady characteristics of vortex structures in front of surface-mounted obstacles

Jiaxin Liu[1], **Yichen Zhu**[1] **and Jinjun Wang**[1]

[1]Fluid Mechanics Key Laboratory of Education Ministry, Beijing University of Aeronautics and Astronautics, Beijing 100191, PR China

Corresponding author: Jinjun Wang, jjwang@buaa.edu.cn

(Received 17 October 2025 UTC; revised 28 April 2026 UTC; accepted 3 June 2026 UTC)

The flow characteristics over isolated surface-mounted obstacles are investigated with time-resolved particle image velocimetry. Three different geometries (square cylinder, circular cylinder, and hemisphere) are considered maintaining the same aspect ratio of 0.5, and are completely submerged in the laminar boundary layer. The height-based Reynolds number is 1530. The time-averaged flow topologies around the three obstacles are quite similar. However, the unsteady characteristics over the square cylinder are significantly stronger than those over the circular cylinder and hemisphere. The vortices upstream of the square cylinder experience periodic amplification and decay while their cores oscillate along the flow direction. These two dynamic mechanisms corresponding to different characteristic frequencies collectively contribute to the oscillation of the entire horseshoe vortex system. Furthermore, a direct correlation between vortex number and flow pattern is established. Three categories of patterns exist in the flow field upstream of the square cylinder, corresponding to different numbers of clockwise vortices. The upstream flow field intermittently switches between these three patterns. In addition, the separation region above the square cylinder exhibits the same high-frequency characteristics as the upstream region due to the spatial oscillations of the horseshoe vortex system. Its low-frequency characteristics, however, originate from the instability of the shear layer at the free end. These findings help fill gaps in the relevant field and contribute to the study on the dynamics of the flow over surface-mounted obstacles.

Key words: vortex dynamics, separated flows, vortex interactions

1. Introduction

Nowadays, the flow around surface-mounted finite height obstacles has been intensely studied due to its wide engineering applications, such as the vortex generators on aircraft, semiconductor heat exchangers, and microfluidic devices. There are various complex flow

© The Author(s), 2026. Published by Cambridge University Press.

https://doi.org/10.1017/jfm.2026.11772 Published online by Cambridge University Press

phenomena occurring around the isolated stationary obstacles, such as flow separation, shear layer interactions, vortex formation, shedding and merging, and interactions between different vortical structures. These flow phenomena are closely related to practical vortex-induced vibrations, resonance, noise generation, and fatigue failure. Although practical engineering scenarios typically involve turbulent boundary layers, the flow structures are difficult to form and develop stably because of turbulence interference. In contrast, the vortex structures in the laminar boundary layer can be better identified and extracted without the complicating effects of freestream turbulence, which is advantageous for understanding the corresponding dynamics. Meanwhile, in experimental studies, typical geometric shapes such as square cylinder, circular cylinder, and hemisphere are commonly used as simplified models to reduce experimental complexity. Thorough investigations of the flow characteristics around such bluff obstacles are essential for improving understanding of the flow physics and developing optimal flow control strategies.

A considerable number of experimental and numerical studies have investigated flow around these obstacles (Castro & Robins 1977; Wang & Zhou 2009; Porteous, Moreau & Doolan 2017; Rastan *et al.* 2017; Zhu *et al.* 2017; Puckert & Rist 2018; Schröder *et al.* 2020; Liu *et al.* 2024, 2025), revealing some of the important coherent structures and the principal parameters governing the flow behavior. For surface-mounted finite square and circular cylinders, Wang *et al.* (2004) and Pattenden, Turnock & Zhang (2005) proposed a comprehensive model for the main flow structures, including the horseshoe vortex (HSV), spanwise vortices, and tip and base vortices. Regarding the hemisphere, Acarlar & Smith (1987) conducted the seminal study on vortical structures around it. They identified the horseshoe vortex system and periodical shedding hairpin vortices in the separated shear layer around a hemisphere using flow visualization techniques. These studies provide effective analytical frameworks for the flow around surface-mounted bluff obstacles.

In general, these flow features are affected by obstacle geometry, aspect ratio ($AR = h/d$, where h and d are the height and width of the obstacle, respectively), the state and thickness of the incoming boundary layer, and Reynolds number (Rostamy *et al.* 2013; Sumner 2013; Yauwenas *et al.* 2019; Essel, Tachie & Balachandar 2021; Hajimirzaie 2023; da Silva *et al.* 2024). Comprehensive reviews of studies on these parameters are well documented by Porteous, Moreau & Doolan (2014) and Forouzi Feshalami *et al.* (2022). As early as 1977, Castro & Robins (1977) conducted one of the earliest experimental investigations of flow around surface-mounted cubes in both uniform and turbulent flows. Based on the measurements of surface pressures and wakes, they found that separating shear layers reattach to the cube surface in a turbulent boundary layer but not in uniform flows, which highlighted the importance of boundary layer characteristics in determining the flow behaviors around surface-mounted obstacles. They also reported that the Reynolds number effect was not significant for the case of turbulent flows. Many related studies further showed that the Reynolds number has a limited influence on the large scale vortical structures around the obstacles, especially on the cylinders with fixed separation points (Okajima 1982; Sakamoto & Arie 1983; Williamson 1996; Bourgeois, Sattari & Martinuzzi 2011). In addition, Diaz-Daniel, Laizet & Vassilicos (2017) and da Silva *et al.* (2024) compared the flow around surface-mounted cubes immersed in laminar and turbulent boundary layers through numerical simulations and found that both the incoming boundary layer state and its thickness may have significant effects on the flow, including the unsteady characteristics, vortex structures, and flow dynamics. Another important parameter is aspect ratio, which fundamentally alters the wake topology. Sakamoto & Arie (1983) conducted systematic experiments on square and circular cylinders with various aspect ratios immersed in turbulent boundary layers. They proposed a critical aspect ratio ($AR_{cr} \approx 2$) below which the antisymmetric Kármán vortex

https://doi.org/10.1017/jfm.2026.11772 Published online by Cambridge University Press

shedding is suppressed and replaced by symmetric arch-type vortices. Thereafter, Sumner, Heseltine & Dansereau (2004), Tsutsui (2012), Porteous *et al.* (2017), and Yauwenas *et al.* (2019) conducted comprehensive experimental and numerical studies on the wake of a finite wall-mounted cylinder with aspect ratios in the range $0.125 < AR < 23$, identifying several shedding regimes. Each shedding regime displayed an additional acoustic tone as AR was increased. However, Wang & Zhou (2009) proposed the steady presence of a unified arch structure with a single dominant frequency within the near-wake region of a square cylinder regardless of AR.

Furthermore, although there are many similarities between the flows around surface-mounted finite square and circular cylinders, there are also some significant differences. Kindree, Shahroodi & Martinuzzi (2018) conducted a comparative experimental study of the flow around a cantilevered circular and square cylinder. They found that significant differences between these two cylinder wakes were observed in both the spectra of the fluctuating fields and the mean flow topology. Hajimirzaie (2023) studied the vortex structures developed in the wake of square and circular cylinders of low aspect ratio $AR = 1$ in a laminar boundary layer. The more complex systems of streamwise structures were observed in the square cylinder compared to the circular cylinder. Overall, previous studies have confirmed that geometric configurations have a significant impact on the flow characteristics.

In addition to the wake, the flow features upstream and at the top of the obstacles have received increasing attention, as they also play an important role in the near-field dynamics. Rostamy *et al.* (2013) experimentally investigated the instantaneous flow field above the free end surfaces of surface-mounted finite circular cylinders and square prisms. The instantaneous velocity fields around both cylinders exhibited flow structures distinct from the mean flow and typically contained more irregularly distributed vortex structures. Essel *et al.* (2021) investigated the variation of time-averaged and instantaneous recirculation regions on the top surface of the surface-mounted cylinders with AR. They found that the leading-edge vortex diminishes as AR increases, while the arch vortex is enhanced near the centre of the cylinder, thereby affecting the downwash of the flow into the near-wake region. Cao *et al.* (2022) topologically described the complete near-wall flow patterns around a surface-mounted square cylinder, specifically flow separation patterns upstream of and above the cylinder. Apsilidis *et al.* (2015) focused on the fluid-structure interactions upstream of a circular cylinder mounted on a smooth wall and studied time-averaged and instantaneous behaviors of the turbulent HSV using planar particle image velocimetry.

As a common feature of surface-mounted cylinders and hemisphere obstacles, HSVs form upstream of the junction of the obstacle with the ground plane from the rolling up of separated shear layers. In engineering applications, HSVs are often associated with significant pressure fluctuations, complex energy exchange, and cavitation (Hou *et al.* 2025). The detailed experiment by Baker (1979) first revealed that, as Reynolds number increases, the flow topology of juncture flow evolves from a single primary HSV to multiple vortices, while the transition from a steady HSV system to an unsteady one also occurs. Meanwhile, the distance of the primary vortex's centre from the obstacle's centre correlates positively with the Reynolds number. Apparently, the unsteady oscillatory behavior of the HSV system would inevitably affect the characteristics of the obstacle wake, and therefore investigations on it are necessary. Baker (1991) analyzed the oscillation of HSV systems around the base of wall-mounted obstacles. They attributed the oscillatory behavior to oscillations of the entire vortex system and the oscillations of the vortex core itself. Wei, Chen & Du (2001) suggested the incessant shedding of HSV and merging or wrapping with each other would cause the oscillatory behavior of

https://doi.org/10.1017/jfm.2026.11772 Published online by Cambridge University Press

the juncture vortex system. Devenport & Simpson (1990) experimentally investigated the behavior of the vortex system upstream of a cylindrical wing mounted normal to a flat surface. They concluded that a complete quasi-periodic routine begins with the presence of a single large-scale HSV, followed by new vortices forming and merging with HSVs, and finally the formation of a new HSV under the action of instability and restarting the cycle. Additionally, they observed that the HSV systems display a bimodal behavior associated with a zeroflow mode and a backflow mode and alternate quasi-periodically between these two states. The zeroflow mode is associated with the vertical ejection of fluid at high velocities and occurs when upstream incoming fluid blocks the backflow, while the backflow mode is characterized by a strong near-wall flow ejected in the direction opposite to the bulk flow. The bimodal unsteadiness has been considered as an important characteristic of junction flows in many studies (Paik, Escauriaza & Sotiropoulos 2007; Apsilidis *et al.* 2015; Kirkil & Constantinescu 2015). However, discussion about the potential existence of additional modes except these two still exists. Hou *et al.* (2025) confirmed the existence of an intermediate mode in addition to the zeroflow and backflow modes, occurring during the transition from the backflow mode to the zeroflow mode.

Although the complex behavior of HSV system in junction flow has been widely studied, most existing work has focused on the junction region between high AR circular cylinders or wall-normal wings and a flat plate. Simpson (2001) and Gazi & Afzal (2020) conducted a detailed review of the relevant investigations, summarizing the formation mechanism and characteristics of vortices in front of the circular cylinder or wing. However, experimental explorations on the unsteady characteristics of HSVs upstream of low AR obstacles, especially for $AR < 1$, are fairly scarce. Previous studies have primarily focused on the characteristics in junction flow of obstacles with larger AR. In contrast, the flow past a low AR obstacle possesses more complex and pronounced unsteady three-dimensional characteristics due to the combined effects of the wall and free end. Additionally, unlike circular cylinders and wings, square cylinders have sharper edges, resulting in fixed separation points, which lead to different characteristics of the surrounding HSV system. Furthermore, previous studies have often investigated the upstream and top flow separately, whereas their interaction remains rather underexplored, particularly for low AR obstacles where this coupling could become especially pronounced.

In conclusion, significant gaps remain in understanding the characteristics of the flow around low AR surface-mounted obstacles, especially for $AR < 1$. Experimental comparisons of the flow in front of different canonical obstacle geometries under the same incoming boundary layer condition are still scarce. Moreover, the unsteady characteristics of the upstream HSV system and the flow at the top for low AR obstacles, as well as their interactions, have not yet been clarified in sufficient detail. In the current work, time-resolved particle image velocimetry (PIV) was employed to quantitatively measure the flow field around the surface-mounted square and circular cylinders with a much lower AR ($AR = 0.5$) immersed in a laminar boundary layer. The flow field around a hemisphere at the same height ($AR = 0.5$) was also measured for comparative analysis. Flow characteristics, including the time-averaged flow pattern, unsteady characteristics, and the interactions between flow structures upstream of and above the obstacles, are analyzed. The unsteady characteristics of the HSV system, including variations in their location, strength, and number, are thoroughly explored, with the aim of providing valuable insights for the dynamics around the surface-mounted obstacles. The paper is structured as follows. Section 2 describes the experimental setup. The mean flow fields of the three obstacles are presented in § 3. Section 4 focuses on the unsteady characteristics over the square cylinder. Finally, § 5 gives the conclusion.

https://doi.org/10.1017/jfm.2026.11772 Published online by Cambridge University Press

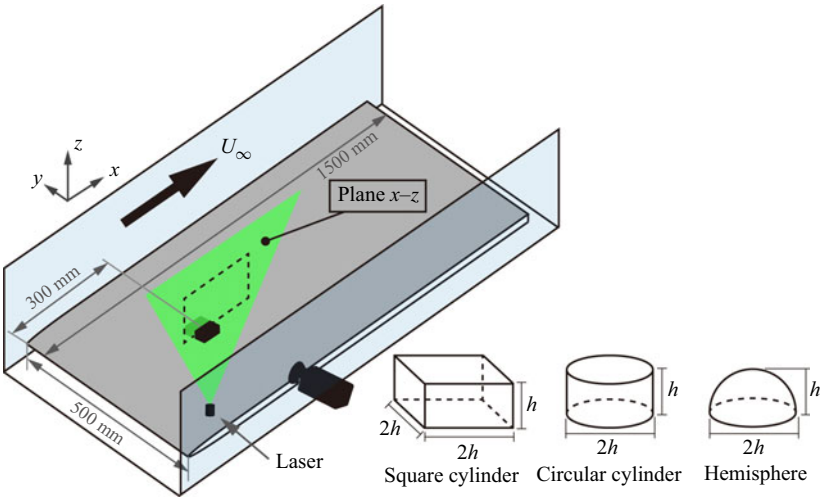


Figure 1. Schematic view of the experimental setup and models.

2. Experimental set-up

The present experiment was conducted in the low-speed water channel of the Institute of Fluid Mechanics at the Beijing University of Aeronautics and Astronautics, with the test section size of 600 mm × 600 mm × 3000 mm (height × width × length). A flat plate of dimensions 500 mm × 15 mm × 1500 mm (height × thickness × length) was installed horizontally 100 mm away from the bottom of the water channel to avoid interference by the channel-wall boundary layer. A 5:1 elliptical leading edge was adopted on the plate to ensure the incoming boundary layer stays in a laminar state. The isolated aluminum obstacle model with smooth surfaces and sharp edges was mounted on the flat plate, with the distance between its centre and the leading edge of the plate being 300 mm. The surfaces of the models were painted black with flatting paint to significantly reduce the amount of reflection. Figure 1 illustrates the experimental setup schematic view and the definition of the coordinates. Three obstacles were examined in the current study, including a square cylinder, a circular cylinder, and a hemisphere, respectively, as schematically shown by the model diagram. To facilitate comparative analysis, all three models adopted the same height of $h = 10$ mm. The diameter of both the circular cylinder and hemisphere is 20 mm, while the length of the base edge of the square cylinder is also 20 mm. As such, the aspect ratio of the current three obstacles is uniformly $AR = 0.5$. The incoming free stream velocity was set to $U_\infty = 154.8\ \mathrm{mm\ s^{-1}}$ with a turbulence intensity less than 0.8 %, so that the Reynolds number based on the height of the obstacle is 1530 ($Re_h = U_\infty h/\nu$, where ν is the kinematic viscosity of the fluid). The origin of the coordinate system is located at the centre of the obstacles, and x and z denote the streamwise and vertical directions, respectively. The corresponding velocity components are denoted as u and w.

The experiment was carried out using a time-resolved two-dimensional PIV to quantitatively measure the flow field in the streamwise-wall-normal (x–z) plane. The target flow field was illumined by a laser sheet with a thickness of approximately 1 mm, coincident with the axial center plane of the obstacles along the streamwise direction. The laser was generated by a dual-head Nd:YAG laser (Beamtech Vlite-Hi-527-50) with an energy output of 50 mJ pulse^{-1}. Hollow glass beads with mean diameters of 5–20 μ m and a density of 1.05 g cm^{-3} were used in the water tunnel as seeding particles. The Stokes number of these tracer particles was approximately 10^{-4}, much

https://doi.org/10.1017/jfm.2026.11772 Published online by Cambridge University Press

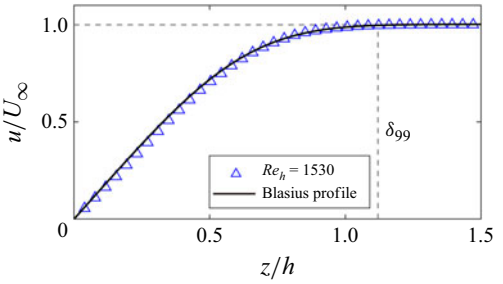


Figure 2. Comparison of the undisturbed boundary layer profile and the Blasius solution.

smaller than unity, demonstrating that these hollow glass beads followed the flow reliably. Particle images were recorded by a high-speed CMOS camera (Photron Fastcam SA2 86 K-M3) equipped with a Nikon lens of 105 mm focal length. The camera has a resolution of 2048×2048 pixels for the field of view, which covered the range $-5.5 < x/h < 2.5$ and $-0.5 < z/h < 3$. The magnification was 0.04 mm pix^{-1}. The sampling frequency was 360 Hz, yielding an average particle displacement of 8 pixels in the free stream. To assess the convergence of the statistical estimates, at least 21 150 PIV snapshots were collected for each obstacle.

The recorded PIV images were preprocessed using the POD-based background removal method, firstly (Mendez *et al.* 2017). Then, the final velocity fields were calculated using the multi-pass iterative Lucas–Kanade (MILK) algorithm (Champagnat *et al.* 2011; Pan *et al.* 2015) from the particle images with four pyramid levels and five Gauss–Newton iterations per level. The interrogation window sizes were set to 32×32 pixels, yielding the vector pitch of 0.34 mm. Following the method of Qu *et al.* (2019) and Zhu, Wang & Liu (2024), the uncertainty in the instantaneous velocity is approximately 1.44 mm s^{-1}, and the corresponding relative uncertainty is below 0.9 %. Additionally, the PIV experiment yields uncertainty of 0.0007 in the time-averaged fields.

According to the study of da Silva *et al.* (2024), the effects of the boundary layer state exist on all flow structures around the surface-mounted obstacles, especially for the HSV system. Therefore, the state of the undisturbed boundary layer was checked in the current work. As shown in figure 2, the time-averaged streamwise velocity profiles without the obstacle fit the Blasius solution very well. Moreover, the shape factor H is 2.56, which is defined as the ratio of the displacement thickness to the momentum thickness of the undisturbed boundary layer. Both indicate that the incoming boundary layer is in a stable laminar state. The boundary layer thickness defined by $0.99U_\infty$ is $\delta_{99} = 1.12h$, which guarantees that the laminar boundary layer submerges the three obstacles.

3. Mean flow fields

Figure 3 presents the time-averaged contour plots of the dimensionless streamwise velocity component superimposed with the mean streamlines to describe the flow topologies over three different obstacles. A topologically similar system of horseshoe vortices was clearly identified upstream of the three obstacles, consisting of three clockwise rotating vortices and an anticlockwise vortex. The three clockwise vortices are referred to as HSV1, HSV2, and HSV3, respectively, according to the distance away from the leading edge of the obstacles. The anticlockwise vortex located between the HSV1 and HSV2 is referred to as secondary HSV (SHSV). Additionally, a distinct separation bubble was observed on the top of both the square and circular cylinders, which is denoted by top separation

https://doi.org/10.1017/jfm.2026.11772 Published online by Cambridge University Press

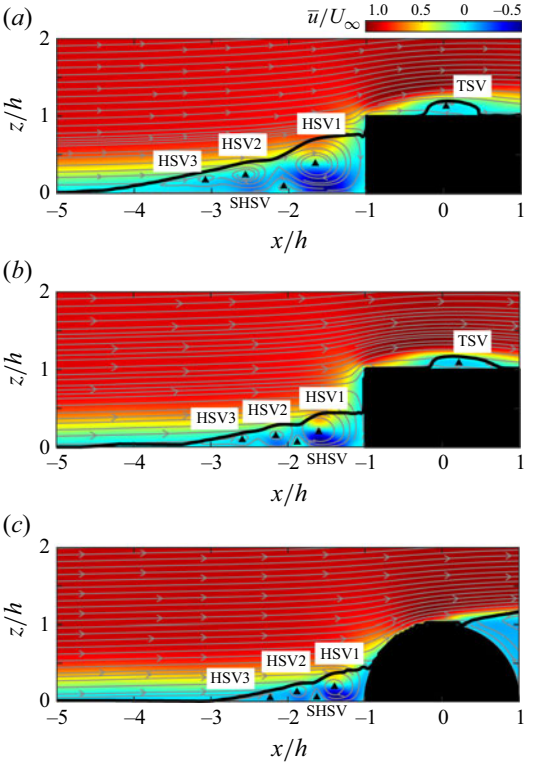


Figure 3. Contours of time-averaged streamwise velocity superimposed with the mean streamlines for the three obstacles: (*a*) square cylinder; (*b*) circular cylinder; (*c*) hemisphere. The solid black lines correspond to the isopleths of $\psi = 0$. The multiple vortex cores are indicated as black triangles respectively.

vortex (TSV) for conciseness. The absence of TSV at the top of the hemisphere was expected, as it possesses a continuous geometry without any sharp-edged platform. All these vortex cores are marked by black triangles. The integral of streamwise mean velocity in the vertical direction $\psi(x, z) = \int_{wall}^{z} U(x, Z)\mathrm{d}Z$ has been calculated, and the isopleth of $\psi = 0$ is plotted in figure 3. Evidently, the isopleth $\psi = 0$ can be considered as the upper bound of the mean separation bubbles in front of and above the obstacles (Fang & Tachie 2019).

As shown in figure 3, the upstream flow separation occurs at approximately $x/h = -4.3, -3.1, -2.8$ for the three obstacles, respectively, and the front stagnation points on the windward side are located at about $z/h = 0.85, 0.75, 0.5$, respectively. Namely, the flow separation onset position is successively delayed from the square cylinder to the circular cylinder and finally to the hemisphere. Correspondingly, the scale of the upstream separation region decreases in sequence. Additionally, the scale of each HSV structure upstream of the three obstacles also decreases sequentially, with a more compact arrangement. This phenomenon can be attributed to the presence of planar free ends on square and circular cylinders that differ from the hemisphere, while the square cylinder additionally features a sharp-edged plane perpendicular to the incoming flow. These geometric features exert a strong blocking effect on the incoming flow, inducing a more pronounced adverse pressure gradient. Consequently, flow separation occurs at a more upstream location, and the front stagnation point shifts upward. Ultimately, the larger separation region and corresponding HSV structures develop.

https://doi.org/10.1017/jfm.2026.11772 Published online by Cambridge University Press

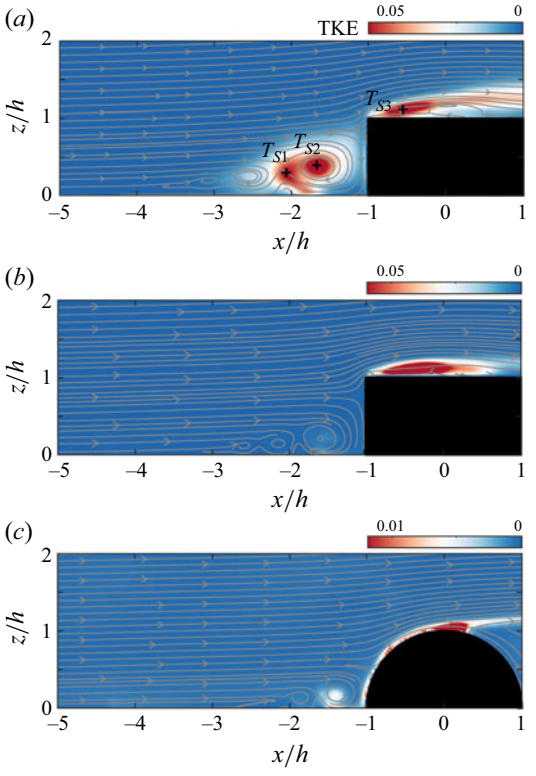


Figure 4. Contours of TKE for the three obstacles: (*a*) square cylinder; (*b*) circular cylinder; (*c*) hemisphere. The local maxima of TKE are indicated as black crosses.

For the top flow, the time-averaged reverse flow regions of both the square and circular cylinders occur at similar streamwise locations, approximately at $x/h = -0.1$, arising from the separated shear layers rolling up and forming separation bubbles. However, the flow reattachment point of the square cylinder ($x/h = 0.5$) is located further upstream than that of the circular cylinder ($x/h = 0.8$), corresponding to a shorter flow separation range. This difference can be attributed to the sharp leading edge perpendicular to the incoming flow of the square cylinder, which is expected to generate a stronger separated shear layer and TSV than above the circular cylinder. The resulting stronger downwash then leads to earlier reattachment of the top flow over the square cylinder.

Figure 4 depicts contours of turbulence kinetic energy (TKE) with local maxima marked by black crosses. Notably, two concentrations of high fluctuating energy are identified upstream of the square cylinder, denoted as T_{S1} and T_{S2}, respectively. The concentration T_{S1} is located between the vortex structures HSV1 and HSV2 and is higher than the core of SHSV, while the concentration T_{S2} is nearly coinciding with the core of HSV1. The values associated with the two local maxima ($\approx 0.055U^2$) are comparable. Similar features have been observed upstream of cylinders by Kirkil & Constantinescu (2015) at a much higher Reynolds number $Re_D = 5 \times 10^5$. They believed that these two maxima are associated with the zeroflow mode and the backflow mode. However, the bimodal behavior, which is characterized by the double-peak probability density function, is not observed in the current result (presented in Appendix). This may be attributed to the status of the incoming boundary layer. As da Silva *et al.* (2024) found in their study of cubes, this signature double-peak PDF of the bimodal behavior in the vicinity of the HSV core is only observed

https://doi.org/10.1017/jfm.2026.11772 Published online by Cambridge University Press

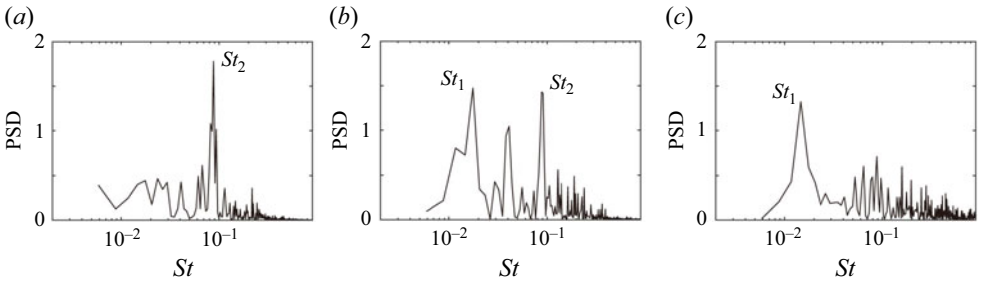


Figure 5. Frequency spectra of streamwise velocity fluctuations upstream of the square cylinder at points T_{S1}, T_{S2}, and T_{S3}, respectively.

for the turbulent boundary layer case. Furthermore, at the current Reynolds number, TKE upstream of the circular cylinder is significantly lower than at the free end, with no distinct peak region present. Similarly, TKE around the hemisphere exhibits low levels. These differences arise because, compared to square cylinder, circular cylinder and hemisphere have smoother curvatures, allowing the HSV system to smoothly wrap around the obstacle and develop downstream. Consequently, the upstream velocity fluctuations are stronger for the square cylinder among the three obstacles, corresponding to the more pronounced unsteady characteristics of the HSV system. In addition, another TKE peak is identified at the top of both the square (figure 4*a*, denoted as T_{S3}) and circular cylinders (figure 4*b*), located between the leading edge of the obstacle and TSV. This region corresponds to the separated shear layer from the free end of cylinders, which rolls up and forms the TSV.

Given the pronounced unsteady characteristics upstream of the square cylinder, the spectral analysis is further conducted on the streamwise velocity fluctuations at the three TKE peaks T_{S1}, T_{S2}, and T_{S3}. As shown in figures 5(*a*) and 5(*c*), there are two different characteristic frequencies $St_2 = 0.09$ and $St_1 = 0.018$ (named according to their magnitude) in the spectra corresponding to T_{S1} and T_{S3}, respectively. Interestingly, both of these two characteristic frequencies are observed in the spectrum at point T_{S2} (figure 5*b*). Among these, the high frequency St_2 is generally comparable with the dimensionless frequencies around the square cylinders with low aspect ratios reported in the literature, for example $St = 0.065 \sim 0.105$ in Sakamoto & Arie (1983), $St = 0.08 \sim 0.09$ in Okajima (1982), $St = 0.09$ in Porteous *et al.* (2017), and $St = 0.08$ in da Silva *et al.* (2022). In addition, Baker (1991) found that the unsteady oscillations of the HSV system consist of two frequency components, namely the secondary oscillation corresponding to $St = 0.01$ and the stronger primary oscillation corresponding to $St = 0.08$, which is similar to the double-frequency behavior observed in the present study. Therefore, it is reasonable to expect that the two characteristic frequencies are associated with distinct mechanisms, while the coexistence of St_1 and St_2 suggests that complex dynamics exist near the HSV1 upstream of the square cylinder. These concerns are explored in detail in the following section.

Figure 6 presents the streamwise variation of multiple vorticity thicknesses for the three obstacles, which is defined as $\delta_\omega = (U_{max} - U_{min})/(\partial U/\partial z)_{max}$, where U_{max} and U_{min} denote the maximum (free stream) and minimum streamwise mean velocity, respectively, in the vertical direction. According to Brown & Roshko (1974) and Fang & Tachie (2019), the vorticity thickness can be adopted to quantify the growth of shear layers. As shown in figure 6(*a*), the upstream shear layer is affected by the HSV system and grows significantly near the front of the square cylinder, even exceeding the height of the square cylinder.

https://doi.org/10.1017/jfm.2026.11772 Published online by Cambridge University Press

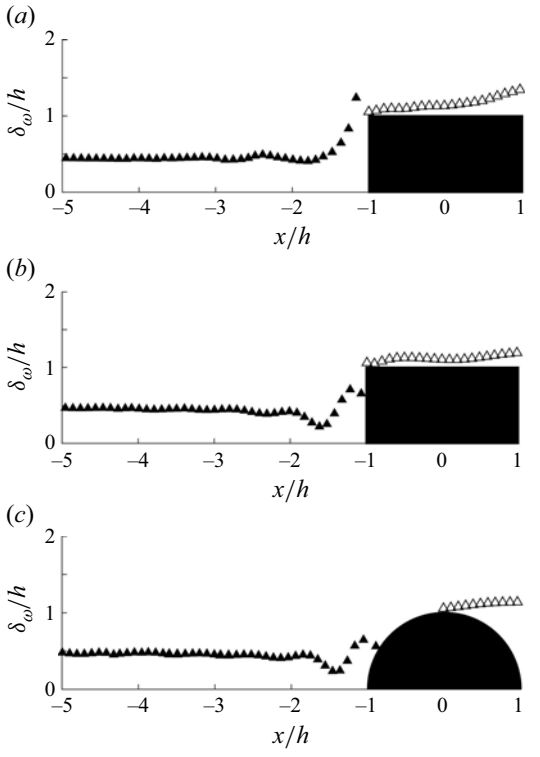


Figure 6. Streamwise variation of vorticity thicknesses δ_ω for the three obstacles: (*a*) square cylinder; (*b*) circular cylinder; (*c*) hemisphere. Solid and hollow triangles correspond to wall shear layer upstream and the shear layer emanating from the free end, respectively.

This is reasonable because the presence of a square cylinder obstructs the incoming flow and creates a significantly adverse pressure gradient, leading to the lift of the upstream shear layer. Meanwhile, another shear layer originates from the leading edge of the square cylinder and develops downstream. Consequently, the two shear layers overlap spatially for the square cylinder with a low aspect ratio. Subsequently, the spatial two-point correlation analysis was performed to further examine the interaction between the upstream and free end shear layers. As shown in figure 7(*a*), an apparent correlated region is observed connecting the upstream and free end flow, indicating clear interaction between the top and upstream flows of the square cylinder. In contrast, the circular cylinder and hemisphere exert less obstruction to the incoming flow, with shear layers in front of both obstacles being lower than the obstacle height. Simultaneously, shear layers developing downstream are present at the free ends of both obstacles. As shown in figure 6(*b*, *c*), the upstream and free end shear layers of the circular cylinder and hemisphere are quite independent. Moreover, the correlated regions remain localized near the free end (figure 7*b*, *c*), suggesting that the interactions between the two shear layers are much weaker in these two cases.

4. Unsteady characteristics over the square cylinder

Based on the above results, among the flow fields over the three obstacles at the current Reynolds number, the flow over the square cylinder exhibits the most pronounced unsteady characteristics, with the strongest interaction between the upstream and top flows. These

https://doi.org/10.1017/jfm.2026.11772 Published online by Cambridge University Press

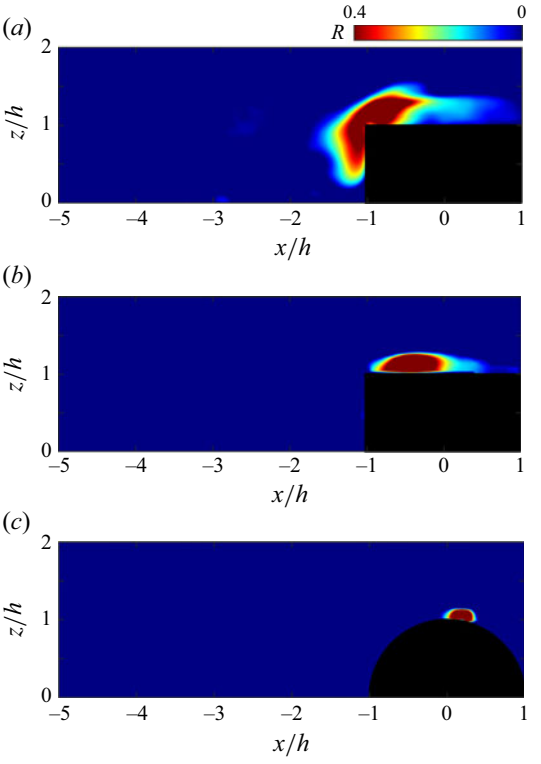


Figure 7. Spatial two-point correlation coefficient of the streamwise velocity fluctuations for the three obstacles: (*a*) square cylinder; (*b*) circular cylinder; and (*c*) hemisphere. The reference point is located at $x/h = -0.9$, $z/h = 1.1$ for square cylinder and circular cylinder, and at $x/h = 0.1$, $z/h = 1.1$ for hemisphere.

findings are also confirmed in subsequent analyses. Therefore, the subsequent study focuses on the unsteady characteristics presented around the square cylinder.

4.1. *Unsteadiness of HSV system*

Firstly, attention is turned to the unsteady characteristics of the HSV system upstream of the square cylinder. Among multiple vortex structures upstream of the obstacles, the three vortices HSV1, SHSV, and HSV2 possess stronger vorticities and are able to be identified robustly in the instantaneous flow field. Also, these three vortices maintain similar relative spatial arrangements. Thus, we track these three representative vortices to quantify the dynamic characteristics of the HSV systems. The Q-criterion (Hunt, Wray & Moin 1988; Jeong & Hussain 1995) is employed to identify vortex structures in this investigation, which is defined as $Q = (\Omega^2 - S^2)/2$, where Ω is the rate of rotation and S is the rate of flow strain. The exact centre locations of the three vortices are identified as the weighted centroids of the Q concentration region separately in each instantaneous snapshot. Specifically, based on their mean locations in the time-averaged flow field, three individual search regions were defined around the corresponding vortices. Within each search region, the weighted centroids of corresponding vortex heads are calculated as $x_c = \int_L x Q \mathrm{d}l / \int_L Q \mathrm{d}l$ and $z_c = \int_L z Q \mathrm{d}l / \int_L Q \mathrm{d}l$, where L is the integral region enclosed by 50 % of the maximum value of the local Q field. The two-dimensional probability density functions (PDF) of the locations of centre of HSV1, SHSV, and HSV2 upstream of the three obstacles are mapped in figure 8, providing a concise way to map the oscillation

https://doi.org/10.1017/jfm.2026.11772 Published online by Cambridge University Press

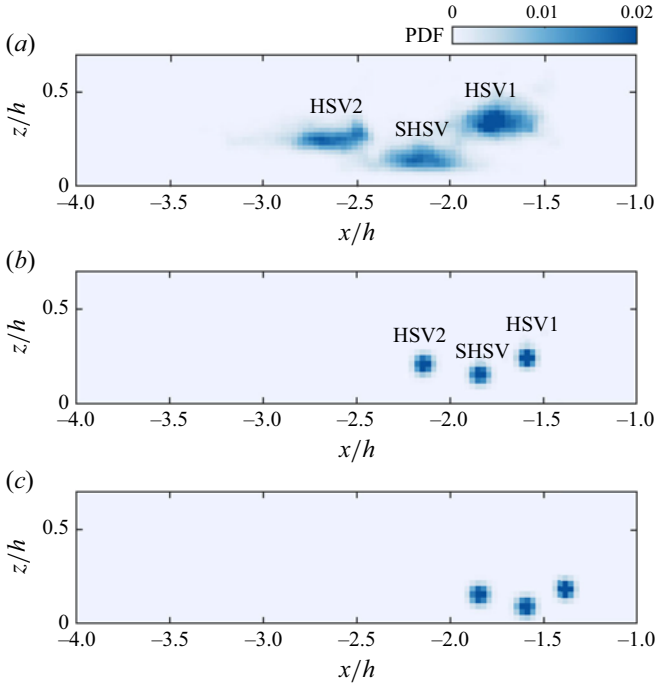


Figure 8. Probability density function distribution of locations of three vortex cores for the three obstacles: (*a*) square cylinder; (*b*) circular cylinder; (*c*) hemisphere.

topology of these vortices simultaneously in time and space (Apsilidis *et al.* 2015). Apparently, the centre locations of the three vortices in front of the square cylinder exhibit more dispersed spatial distributions, indicating that the upstream HSV system is highly dynamic. In contrast, the vortex cores upstream of the circular cylinder and hemisphere maintain relatively fixed positions, further confirming the absence of noticeable unstable oscillations in HSV system in these two cases. For the square cylinder case, locations of HSV1, SHSV, and HSV2 all exhibit significant oscillations in both the streamwise and vertical directions. Specifically, the streamwise oscillation extents of the three vortices upstream of the square cylinder are roughly the same, approximately $0.45h$, whereas the corresponding vertical oscillation extents are $0.15h$ for HSV1, $0.1h$ for SHSV, and $0.09h$ for HSV2, respectively. The fact that the streamwise oscillation amplitudes of the three vortices are considerably higher than the vertical ones indicates that the streamwise oscillations of HSV structures upstream of the square cylinder are dominant. Furthermore, the PDF concentration regions of the three vortex centres remain well separated, each clustered within the streamwise ranges of $x/h = -2 \sim -1.5$ (HSV1), $-2.4 \sim -2$ (SHSV), and $-2.9 \sim -2.4$ (HSV2), respectively, and there is limited overlap among them. This suggests that the three representative vortices oscillate independently upstream of the square cylinder, whereas the vortex merging events among them are not common.

Moreover, we assess cross-correlation between the streamwise position of the core of three vortices upstream of the square cylinder (denoted as x_{HSV1}, x_{SHSV} and x_{HSV2}, respectively). As shown in figure 9(*a*), there are clear positive correlations between each pair of the three vortices. Furthermore, the cross-correlation curves reach their peaks at the zero-time lag, indicating that there is no phase difference between the variation of streamwise positions of these three vortices. Among them, the frequency spectrum of x_{HSV1} is plotted in figure 9(*b*), possessing a sharp peak at $St_2 = 0.09$. This indicates

https://doi.org/10.1017/jfm.2026.11772 Published online by Cambridge University Press

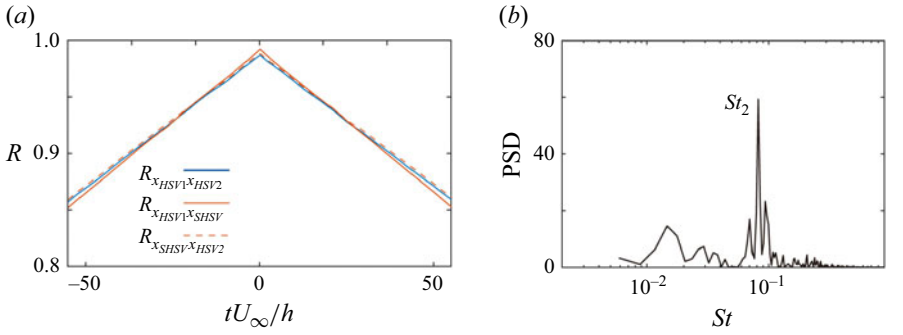


Figure 9. (*a*) Cross-correlations between the streamwise positions of the core of three vortices, respectively. (*b*) Frequency spectrum of x_{HSV1}.

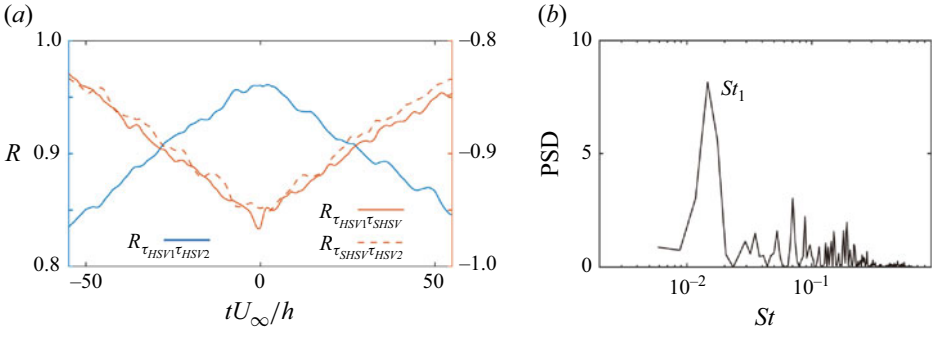


Figure 10. (*a*) Cross-correlations between the tangential velocity of the three vortices, respectively. (*b*) Frequency spectrum of τ_{HSV1}.

that the aforementioned three major HSV vortex structures undergo periodic streamwise oscillations at frequency St_2. In other words, the mechanism corresponding to the high-frequency feature St_2 in the upstream region of the square cylinder is the spatial oscillation of the HSV system.

In addition to spatial oscillations, variations in the vortex strength are also worth studying. In the current work, the tangential velocity of the corresponding vortex is used to quantify their instantaneous strength. The tangential velocity (denoted as τ_{HSV1}, τ_{SHSV} and τ_{HSV2}, respectively) is defined as the average tangential velocity along the boundary of the vortex core, which is 50 % of the maximum value of the local Q field. Figure 10 provides the cross-correlation between them, as well as the spectrum of τ_{HSV1}. It is observed that the tangential velocities of HSV1 and HSV2 with the same rotation direction are positively correlated. Conversely, the tangential velocity of SHSV is negatively correlated with theirs. This indicates that the strength of clockwise rotating vortices and the anticlockwise vortex alternates over time, demonstrating mutual suppression. Additionally, τ_{HSV1} possesses a distinct characteristic frequency $St_1 = 0.018$ as shown in figure 10(*b*), suggesting that HSV1 undergoes periodic amplification and decay while oscillating in the streamwise direction. Due to the high correlation, the strengths of these three vortices all manifest periodic variations at low frequency. Namely, the strength variation behaviors of the HSVs in front of the square cylinder correspond with characteristic frequency St_1. Recalling figure 5, the coexistence of two characteristic frequencies at point T_{S2} can be attributed to the combined effects of the position oscillation

https://doi.org/10.1017/jfm.2026.11772 Published online by Cambridge University Press

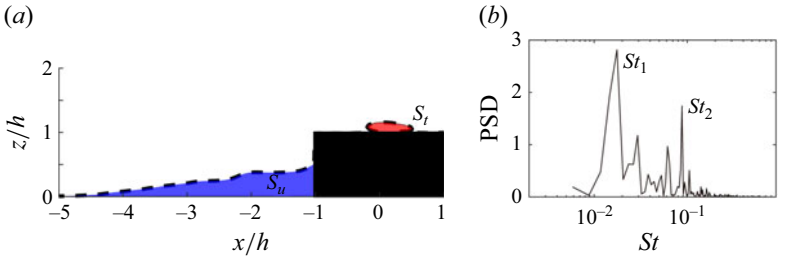


Figure 11. (*a*) Schematic diagram of the size of reverse flow area upstream of and above the square cylinder. (*b*) Frequency spectrum of S_u.

and strength variation of HSV1. Yet the vertical range of SHSV is closer to the wall, and its strength variation has scant effect on flow near point T_{S1}. Since the point T_{S1} is the saddle point between HSV1 and HSV2, position oscillations of vortices have a primary influence on the flow around it. Therefore, point T_{S1} mainly exhibits high-frequency characteristics.

For completeness, the unsteady characteristic of the entire HSV system upstream of the square cylinder is also studied, in addition to the three easily traceable vortex structures mentioned above. As another important metric, the size of the separation region upstream of the square cylinder is closely associated with the dynamic behavior of multiple HSVs. Herein, the instantaneous reverse flow area (the straightforward summation of areas with $u < 0$, denoted as S_u) is used to quantify the size of the instantaneous entire separated region upstream of the square cylinder, namely the area of the blue region in figure 11(*a*). To assess the temporal characteristics of the whole separated region, figure 11(*b*) provides the frequency spectrum of S_u. Clearly, S_u possesses two characteristic frequencies at $St_1 = 0.018$ and $St_2 = 0.09$. This indicates that the aforementioned two dynamic mechanisms collectively contribute to the oscillation of the entire HSV system upstream of the square cylinder.

4.2. *Statistics of vortex number*

In addition to position and strength, the number of HSV vortices upstream of the square cylinder also exhibits complex temporal variations at the current Reynolds number. Compared to clockwise vortex structures, anticlockwise vortices are weaker and more difficult to capture. Therefore, this section discusses the number of clockwise HSV structures in front of the square cylinder in detail. It should be noted that the usual identification criteria based on local quantities (such as Q-criterion) are quite intermittent for structures such as HSV3 further upstream due to small scales. To avoid this limitation, the Γ_1 vortex identification function (Graftieaux, Michard & Grosjean 2001) is employed to pinpoint the vortex, which is able to robustly characterize the small-scale vortices based on only the topology of the velocity field. Figure 12(*a*) gives the statistics of the number of instantaneous clockwise vortices at different snapshots. It is indicated that all samples can be classified into three categories based on the number of clockwise vortices, corresponding to 2, 3, and 4 clockwise vortices, respectively. For conciseness, these three categories are referred to as N2, N3, and N4 in the following text.

To further investigate the flow pattern corresponding to different categories, conditional averaging is applied to the samples under three conditions. As shown in figure 13, the flow pattern corresponding to pattern N2 manifests the simplest organization, consisting of only two clockwise vortices, HSV1 and HSV2, as well as an anticlockwise vortex, SHSV, between them. Notably, the streamwise range of the HSV2 is quite large, spanning about $x/h = -3.3 \sim -2.3$. Pattern N3 (figure 13*b*) features a contracted streamwise extent

https://doi.org/10.1017/jfm.2026.11772 Published online by Cambridge University Press

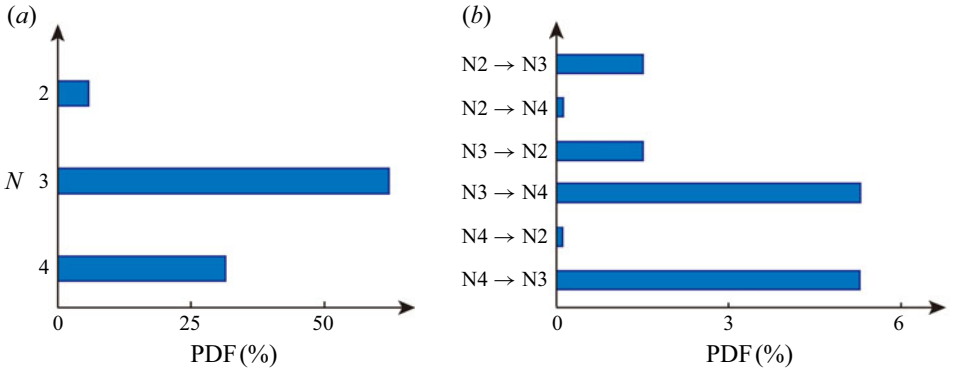


Figure 12. (*a*) Statistics of the number of instantaneous clockwise vortices in front of the square cylinder. (*b*) Statistics of the switching process between different patterns.

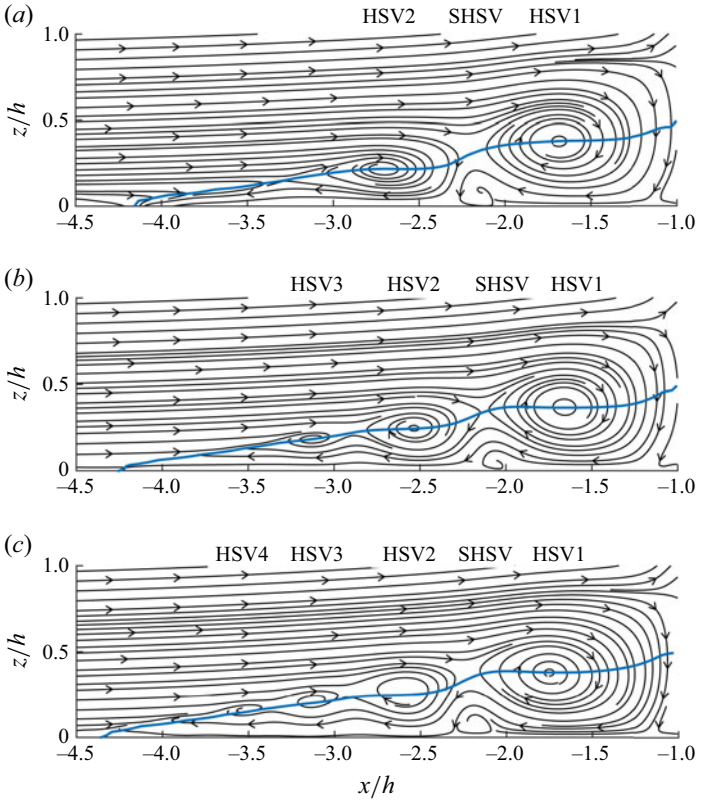


Figure 13. Conditional averaged flow fields. (*a*), (*b*), and (*c*) correspond to pattern N2, N3, and N4, respectively. The superimposed blue lines are isopleth $U = 0$.

of HSV2 accompanied by the emergence of a third clockwise vortex (HSV3) further upstream. Since the pattern N3 is the most frequently observed configuration, as evidenced by figure 12(*a*), its topology is very similar to the time-averaged flow field shown in figure 3, indicating its dominant role in determining the mean flow characteristics. For the pattern N4 (figure 13*c*), a fourth clockwise vortex structure HSV4 appears upstream of HSV3. Nevertheless, the intensity of HSV4 is very weak and difficult to detect in the

https://doi.org/10.1017/jfm.2026.11772 Published online by Cambridge University Press

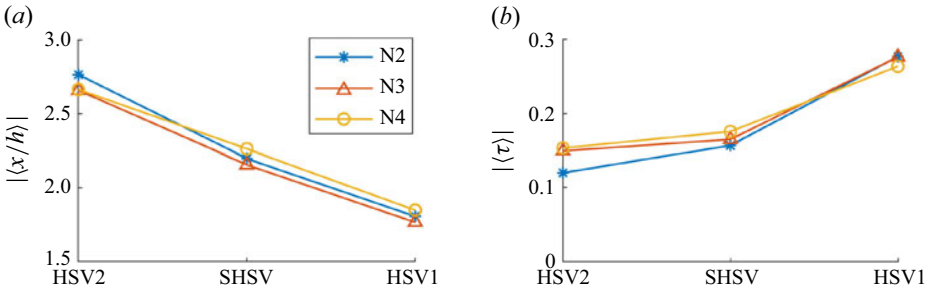


Figure 14. Conditional averaged the streamwise position (*a*) and tangential velocity (*b*) of three vortex structures HSV1, SHSV, and HSV2, at three patterns. Both figures give the absolute values for intuitiveness.

time-averaged flow field, although the N4 pattern is the second most common pattern. Additionally, the switching process between patterns is also statistically analyzed. Note that only the PDF of pattern changes is counted, while consecutive frames corresponding to the same pattern are ignored. As shown in figure 12(*b*), the most common transition occurs between patterns N3 and N4, followed by transitions between N2 and N3. The probability of a direct transition between N2 and N4 is extremely low, almost negligible. In summary, the flow field upstream of the square cylinder intermittently switches between these three patterns.

Furthermore, as intuitively observed in figure 13, the length of the upstream separation region of the square cylinder is directly proportional to the number of clockwise vortices. That is, the more vortex structures there are in the HSV system, the larger the separation region. This is reasonable because only with a sufficient separation region can more vortex structures be accommodated.

To gain a deeper understanding of the three patterns, the streamwise position and tangential velocity of three main vortex structures (HSV1, SHSV, and HSV2) are conditionally averaged. For intuitiveness, figure 14(*a*) gives the absolute values of the conditional averaged streamwise positions, which indicate the distance from the conditional averaged vortex core to the origin (angular brackets $\langle \cdot \rangle$ represent conditional averaging). Since N3 is the dominant pattern at the current Reynolds number, we consider it as the baseline pattern. As shown in figure 14, the conditional averaged distances between the three vortices and the origin are minimum in pattern N3, while their corresponding tangential velocities are intermediate compared to the other patterns. When the number of clockwise vortices deviates from the baseline, whether more or fewer, HSV1, SHSV, and HSV2 all move away from the square cylinder. For pattern N2, the tangential velocities of both HSV2 and SHSV decrease compared to baseline N3. This reduction, coupled with the distinct larger scale of HSV2 and SHSV in pattern N2, suggests that the dissipative effects acting on these vortices are relatively weaker in pattern N2, leading to a strong coherence within the vortex structures. During the transition from pattern N2 to N3, the original HSV2 undergoes instability, ultimately breaking down and forming smaller-scale structures HSV2 and HSV3. Conversely, the merger of HSV2 and HSV3 has been witnessed during the transition from N3 to N2, forming a large-scale HSV2 structure. A similar spatial trend is observed in pattern N4, where both HSV2 and SHSV proceed to move further away from the square cylinder. However, unlike the pattern N2, the tangential velocities of these vortices in pattern N4 surpass those in pattern N3, suggesting a heightened susceptibility to dissipation and instability. The scales of HSV2 and HSV3 further decrease compared to N3, and the further cascade of instability

https://doi.org/10.1017/jfm.2026.11772 Published online by Cambridge University Press

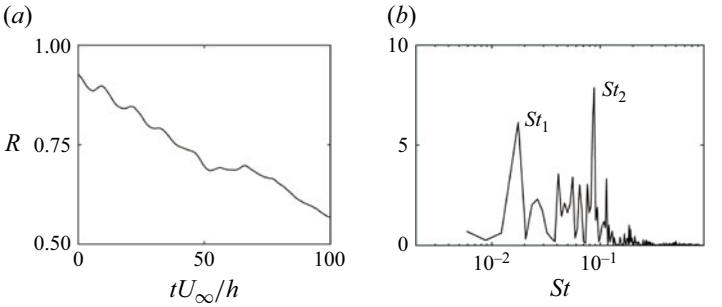


Figure 15. (*a*) Cross-correlations of S_u and S_t. (*b*) Frequency spectrum of S_t.

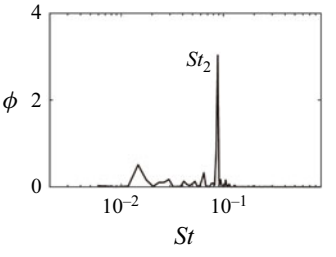


Figure 16. The phase-shifted co-spectrum $\phi(f, 0)$.

promotes the generation of HSV4. Meanwhile, the transition from pattern N4 to N3 occurs via the vortex merging between HSV4 and HSV3.

4.3. *Interaction between HSV and TSV*

We now turn our attention to the unsteady characteristics of the separation bubble on the top of the square cylinder, namely TSV, and the interaction between HSV systems and TSV. This interaction between vortex systems is a unique phenomenon specific to the square cylinder among the three obstacles, as indicated above. Considering the small scale of instantaneous TSV, the area of reverse flow above the square cylinder is calculated to quantify the size of TSV (denoted as S_t), indicated by the area of the red region in figure 11(*a*). Figure 15(*a*) presents the temporal cross-correlation of S_u and S_t. The value of $R(0)$ is as high as 0.91, which is indicative of a good synchronization of S_u and S_t. Meanwhile, the spectrum of S_t is plotted in figure 15(*b*), indicating that S_t possesses two characteristic frequencies identical to S_u at $St_1 = 0.018$ and $St_2 = 0.09$.

In addition, the phase-shifted co-spectrum is adopted to further evaluate the contribution to the peak value of the cross-correlation $R(t)$ from different frequencies, which is defined as:

$$\phi(f, t) = \overline{\widehat{S_u}(f)[\widehat{S_t}(f)\exp(2\pi ift)]^*} + \overline{\widehat{S_t}^*(f)\widehat{S_u}(f)\exp(2\pi ift)}. \tag{4.1}$$

Here, $i = \sqrt{-1}$, and $\widehat{(\cdot)}$ and $(\cdot)^*$ denote the Fourier transformed coefficient and complex conjugate, respectively. Since the peak of $R(t)$ is reached at $t = 0$ value, the $\phi(f, 0)$ is plotted in figure 16. It is seen that the ϕ possesses a distinct peak at $St_2 = 0.09$, while trivial magnitudes at the other frequencies including $St_1 = 0.018$. This indicates that the peak value of the cross-correlation coefficient is primarily governed by the higher frequency St_2, while the contribution of the lower frequency St_1 is limited. Interestingly, the peak

https://doi.org/10.1017/jfm.2026.11772 Published online by Cambridge University Press

value $St_2 = 0.09$ exactly coincides with the characteristic frequency of spatial oscillation of the HSV system. Therefore, both the separation regions upstream of and above the square cylinder are influenced by spatial oscillations originating from the HSV system, experiencing a high-frequency oscillation at $St_2 = 0.09$. However, although both S_u and S_t exhibit distinct peaks at frequency St_1, the low-frequency characteristics of these two separation regions may be attributed to different sources. Based on figure 5(*c*), the low-frequency characteristics are observed in the shear layer generated at the free end of the square cylinder. Therefore, the low-frequency characteristics of the separation bubble at the top of the square cylinder may be influenced by the instability of the shear layer at the free end of the square cylinder.

5. Conclusion

The present study conducted time-resolved two-dimensional PIV to investigate the flow characteristics around surface-mounted obstacles at Reynolds number $Re_h = 1530$. Three different geometries (square cylinder, circular cylinder, and hemisphere) are considered maintaining the same aspect ratio of 0.5 and height of 10 mm, and are completely submerged in the laminar boundary layer of $\delta/h = 1.12$. The novelty of this study lies in experimentally comparing the effects of geometry on the flow characteristics in front of surface-mounted obstacles at such a low AR. The unsteady characteristics and corresponding dynamic mechanisms upstream of and above the square cylinder are revealed, as well as the interactions between them. Meanwhile, a direct correlation between vortex number and flow pattern has been established.

The time-averaged flow topologies around the three obstacles are quite similar. However, the upstream region of the square cylinder is significantly larger, forming larger-scale HSV structures. Simultaneously, the unsteady characteristics over the square cylinder are markedly stronger than those over the circular cylinder and hemisphere, with higher TKE amplitudes. Furthermore, pronounced upstream-top flow interactions exist in the square cylinder case, which are not evident in the flow around the circular cylinder and hemisphere.

Two dynamic mechanisms have been observed upstream of the square cylinder, corresponding to two different characteristic frequencies. The mechanism corresponding to the high-frequency feature St_2 is the spatial oscillation of the HSV system. The cores of three major HSV vortex structures (HSV1, HSV2, and SHSV) that can be robustly identified undergo periodic streamwise oscillations. The streamwise locations of their cores exhibit high positive correlations with no phase difference. Meanwhile, the strength variation behaviors of the HSVs correspond with characteristic low frequency St_1; that is, the vortices upstream of the square cylinder experience periodic amplification and decay while oscillating along the streamwise direction. Differently, the strength of clockwise and anticlockwise vortices alternates over time, indicating mutual suppression. Additionally, the unsteady characteristic of the entire HSV system upstream of the square cylinder is also investigated. The temporal characteristics of the whole separated region possess two characteristic frequencies corresponding to St_1 and St_2, which confirms that the aforementioned two dynamic mechanisms collectively contribute to the oscillation of the entire HSV system upstream of the square cylinder.

Moreover, based on the different numbers of clockwise vortices in the instantaneous flow field, all samples can be classified into three categories corresponding to 2, 3, and 4 clockwise vortices, respectively. The flow patterns corresponding to each category are obtained through conditional averaging. Statistical analysis of the switching process between patterns reveals that the flow field upstream of the square cylinder intermittently

https://doi.org/10.1017/jfm.2026.11772 Published online by Cambridge University Press

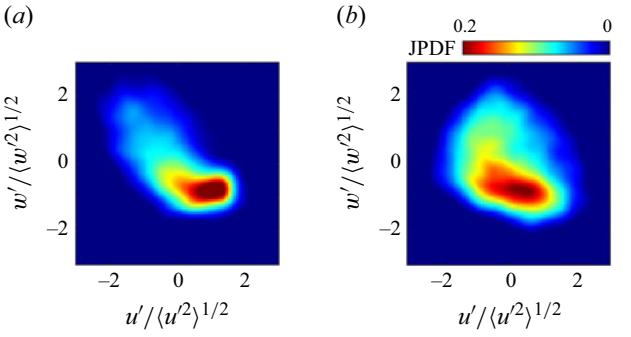


Figure 17. JPDF at point (*a*) T_{S1} and (*b*) T_{S2} upstream of the square cylinder, respectively.

switches between these three categories. However, the probability of a direct transition between N2 and N4 is extremely low, and all pattern switches involve the baseline pattern N3. When the number of clockwise vortices in the instantaneous flow field deviates from the baseline, whether more or fewer, the three main structures (HSV1, SHSV, and HSV2) all move away from the square cylinder. But their tangential velocities increase with the number of clockwise vortices, suggesting a heightened susceptibility to dissipation and instability. These findings establish a direct correlation between vortex number and flow pattern, providing new insights into the spatiotemporal characteristics of HSV system upstream of the bluff bodies.

Finally, the unsteady characteristics of TSV and its interactions with HSV systems are explored. Both the separation regions upstream of and above the square cylinder are influenced by spatial oscillations corresponding to the high frequency St_2 originating from the HSV system. Differently, the low-frequency features in the region above the square cylinder originate from the instability of the shear layer at the free end. In summary, the present work enhances the understanding of the oscillatory mechanisms over the surface-mounted obstacles, providing valuable insights for future research on different geometric obstacles with small *AR*.

Funding. This work was supported by the National Natural Science Foundation of China (no. 11721202).

Declaration of interests. The authors report no conflict of interest.

Appendix. Joint PDF analysis

Figure 17 presents the joint probability density functions (JPDF) of the local streamwise and vertical velocity fluctuations at the two TKE peaks T_{S1} and T_{S2} upstream of the square cylinder (refer to figure 4). The resulting JPDF distributions exhibit single continuous clusters rather than two distinctly separated clusters. This observation supports the absence of a typical bimodal behavior (characterized by double-peak PDF) upstream of the square cylinder immersed in the laminar boundary layer. These distributions may also serve as a useful reference for future studies.

References

Acarlar, M.S. & Smith, C.R. 1987 A study of hairpin vortices in a laminar boundary layer. Part 1. Hairpin vortices generated by a hemisphere protuberance. *J. Fluid Mech.* **175**, 1–43.

Apsilidis, N., Diplas, P., Dancey, C.L. & Bouratsis, P. 2015 Time-resolved flow dynamics and Reynolds number effects at a wall–cylinder junction. *J. Fluid Mech.* **776**, 475–511.

Baker, C.J. 1979 The laminar horseshoe vortex. *J. Fluid Mech.* **95** (2), 347–367.

https://doi.org/10.1017/jfm.2026.11772 Published online by Cambridge University Press

BAKER, C.J. 1991 The oscillation of horseshoe vortex systems. *J. Fluids Engng* **113** (3), 489–495.
BOURGEOIS, J.A., SATTARI, P. & MARTINUZZI, R.J. 2011 Alternating half-loop shedding in the turbulent wake of a finite surface-mounted square cylinder with a thin boundary layer. *Phys. Fluids* **23**, 095101.
BROWN, G.L. & ROSHKO, A. 1974 On density effects and large structure in turbulent mixing layers. *J. Fluid Mech.* **64** (4), 775–816.
CAO, Y., TAMURA, T., ZHOU, D., BAO, Y. & HAN, Z. 2022 Topological description of near-wall flows around a surface-mounted square cylinder at high Reynolds numbers. *J. Fluid Mech.* **933**, A39.
CASTRO, I.P. & ROBINS, A.G. 1977 The flow around a surface-mounted cube in uniform and turbulent streams. *J. Fluid Mech.* **79** (2), 307–335.
CHAMPAGNAT, F., PLYER, A., LE BESNERAIS, G., LECLAIRE, B., DAVOUST, S. & LE SANT, Y. 2011 Fast and accurate PIV computation using highly parallel iterative correlation maximization. *Exp Fluids* **50** (4), 1169–1182.
DEVENPORT, W.J. & SIMPSON, R.L. 1990 Time-dependent and time-averaged turbulence structure near the nose of a wing-body junction. *J. Fluid Mech.* **210**, 23–55.
DIAZ-DANIEL, C., LAIZET, S. & VASSILICOS, J.C. 2017 Direct numerical simulations of a wall-attached cube immersed in laminar and turbulent boundary layers. *Intl J. Heat Fluid Flow* **68**, 269–280.
ESSEL, E.E., TACHIE, M.F. & BALACHANDAR, R. 2021 Time-resolved wake dynamics of finite wall-mounted circular cylinders submerged in a turbulent boundary layer. *J. Fluid Mech.* **917**, A8.
FANG, X. & TACHIE, M.F. 2019 On the unsteady characteristics of turbulent separations over a forward–backward-facing step. *J. Fluid Mech.* **863**, 994–1030.
FOROUZI FESHALAMI, B., HE, S., SCARANO, F., GAN, L. & MORTON, C. 2022 A review of experiments on stationary bluff body wakes. *Phys. Fluids* **34** (1), 011301.
GAZI, A.H. & AFZAL, M.S. 2020 A review on hydrodynamics of horseshoe vortex at a vertical cylinder mounted on a flat bed and its implication to scour at a cylinder. *Acta Geophys.* **68** (3), 861–875.
GRAFTIEAUX, L., MICHARD, M. & GROSJEAN, N. 2001 Combining PIV, POD and vortex identification algorithms for the study of unsteady turbulent swirling flows. *Meas. Sci. Technol.* **12** (9), 1422–1429.
HAJIMIRZAIE, S.M. 2023 Experimental observations on flow characteristics around a low-aspect-ratio wall-mounted circular and square cylinder. *Fluids* **8** (1), 32.
HOU, Z., TANG, Z., FAN, Z., CHEN, L., LIU, J., TIAN, H., CHENG, X. & JIANG, N. 2025 Multimodal behavior of turbulent junction flow. *Phys. Fluids* **37** (5), 055133.
HUNT, J.C.R., WRAY, A.A. & MOIN, P. 1988 *Eddies, Streams, and Convergence Zones in Turbulent Flows*, pp. 193–208. Center for Turbulence Research.
JEONG, J. & HUSSAIN, F. 1995 On the identification of a vortex. *J. Fluid Mech.* **285**, 69–94.
KINDREE, M.G., SHAHROODI, M. & MARTINUZZI, R.J. 2018 Low-frequency dynamics in the turbulent wake of cantilevered square and circular cylinders protruding a thin laminar boundary layer. *Exp. Fluids* **59** (12), 186.
KIRKIL, G. & CONSTANTINESCU, G. 2015 Effects of cylinder Reynolds number on the turbulent horseshoe vortex system and near wake of a surface-mounted circular cylinder. *Phys. Fluids* **27** (7), 075102.
LIU, J., WANG, J., ZHU, Y. & PAN, C. 2024 Vortex dynamics in the near wake of a surface-mounted hemisphere. *Phys. Fluids* **36** (1), 013619.
LIU, J., ZHU, Y. & WANG, J. 2025 The near-wake vortex dynamics of a wall-mounted hemisphere measured with tomographic particle image velocimetry. *J. Fluid Mech.* **1012**, A7.
MENDEZ, M.A., RAIOLA, M., MASULLO, A., DISCETTI, S., IANIRO, A., THEUNISSEN, R. & BUCHLIN, J.M. 2017 POD-based background removal for particle image velocimetry. *Exp. Therm. Fluid Sci.* **80**, 181–192.
OKAJIMA, A. 1982 Strouhal numbers of rectangular cylinders. *J. Fluid Mech.* **123**, 379–398.
PAIK, J., ESCAURIAZA, C. & SOTIROPOULOS, F. 2007 On the bimodal dynamics of the turbulent horseshoe vortex system in a wing-body junction. *Phys. Fluids* **19** (4), 045107.
PAN, C., XUE, D., XU, Y., WANG, J.J. & WEI, R.J. 2015 Evaluating the accuracy performance of Lucas–Kanade algorithm in the circumstance of PIV application. *Sci. China Phys. Mech. Astron.* **58** (10), 104704.
PATTENDEN, R.J., TURNOCK, S.R. & ZHANG, X. 2005 Measurements of the flow over a low-aspect-ratio cylinder mounted on a ground plane. *Exp. Fluids* **39** (1), 10–21.
PORTEOUS, R., MOREAU, D.J. & DOOLAN, C.J. 2014 A review of flow-induced noise from finite wall-mounted cylinders. *J. Fluids Struct.* **51**, 240–254.
PORTEOUS, R., MOREAU, D.J. & DOOLAN, C.J. 2017 The aeroacoustics of finite wall-mounted square cylinders. *J. Fluid Mech.* **832**, 287–328.
PUCKERT, D.K. & RIST, U. 2018 Experiments on critical Reynolds number and global instability in roughness-induced laminar–turbulent transition. *J. Fluid Mech.* **844**, 878–904.

https://doi.org/10.1017/jfm.2026.11772 Published online by Cambridge University Press

QU, Y., WANG, J., FENG, L. & HE, X. 2019 Effect of excitation frequency on flow characteristics around a square cylinder with a synthetic jet positioned at front surface. *J. Fluid Mech.* **880**, 764–798.
RASTAN, M.R., SOHANKAR, A. & ALAM, M.M. 2017 Low-Reynolds-number flow around a wall-mounted square cylinder: flow structures and onset of vortex shedding. *Phys. Fluids* **29** (10), 103601.
ROSTAMY, N., SUMNER, D., BERGSTROM, D.J. & BUGG, J.D. 2013 Instantaneous flow field above the free end of finite-height cylinders and prisms. *Intl J. Heat Fluid Flow* **43**, 120–128.
SAKAMOTO, H. & ARIE, M. 1983 Vortex shedding from a rectangular prism and a circular cylinder placed vertically in a turbulent boundary layer. *J. Fluid Mech.* **126**, 147–165.
SCHRÖDER, A., WILLERT, C., SCHANZ, D., GEISLER, R., JAHN, T., GALLAS, Q. & LECLAIRE, B. 2020 The flow around a surface mounted cube: a characterization by time-resolved PIV, 3D shake-the-box and LBM simulation. *Exp. Fluids* **61** (9), 189.
DA SILVA, B.L., SUMNER, D. & BERGSTROM, D.J. 2022 Mean and dynamic aspects of the wakes of a surface-mounted cube and block. *J. Fluids Engng* **144** (1), 011302.
DA SILVA, B.L., SUMNER, D. & BERGSTROM, D.J. 2024 Revisiting the surface-mounted cube: an updated perspective of the near wake and near-wall flow field. *Intl J. Heat Fluid Flow* **106**, 109288.
SIMPSON, R.L. 2001 Junction flows. *Annu. Rev. Fluid Mech.* **33** (1), 415–443.
SUMNER, D. 2013 Flow above the free end of a surface-mounted finite-height circular cylinder: a review. *J. Fluids Struct.* **43**, 41–63.
SUMNER, D., HESELTINE, J.L. & DANSEREAU, O.J.P. 2004 Wake structure of a finite circular cylinder of small aspect ratio. *Exp. Fluids* **37** (5), 720–730.
TSUTSUI, T. 2012 Flow around a cylindrical structure mounted in a plane turbulent boundary layer. *J. Wind Engng Ind. Aerodyn.* **104–106**, 239–247.
WANG, H.F., ZHOU, Y., CHAN, C.K., WONG, W.O. & LAM, K.S. 2004 Flow structure around a finite-length square prism. In *15th Australasian Fluid Mechanics Conference*. The University of Sydney.
WANG, H.F. & ZHOU, Y. 2009 The finite-length square cylinder near wake. *J. Fluid Mech.* **638**, 453–490.
WEI, Q.D., CHEN, G. & DU, X.D. 2001 An experimental study on the structure of juncture flows. *J. Vis. Japan* **3** (4), 341–348.
WILLIAMSON, C.H.K. 1996 Vortex dynamics in the cylinder wake. *Annu. Rev. Fluid Mech.* **28** (1996), 477–539.
YAUWENAS, Y., PORTEOUS, R., MOREAU, D.J. & DOOLAN, C.J. 2019 The effect of aspect ratio on the wake structure of finite wall-mounted square cylinders. *J. Fluid Mech.* **875**, 929–960.
ZHU, H.-Y., WANG, C.-Y., WANG, H.-P. & WANG, J.-J. 2017 Tomographic PIV investigation on 3D wake structures for flow over a wall-mounted short cylinder. *J. Fluid Mech.* **831**, 743–778.
ZHU, Y., WANG, J. & LIU, J. 2024 Tip effects on three-dimensional flow structures over low-aspect-ratio plates: mechanisms of spanwise fluid transport. *J. Fluid Mech.* **983**, A35.

https://doi.org/10.1017/jfm.2026.11772 Published online by Cambridge University Press